

# BEAM MEASUREMENTS OF A LARGE SOLID-ANGLE BEAM LOSS MONITOR IN THE APS\*

B.X. Yang, W. Berg, J. Dooling, A. Pietryla, A. Brill, and L. Erwin  
Advanced Photon Source, Argonne National Laboratory, Argonne, IL 60439, USA.

## Abstract

For reliable radiation dosimetry of undulator magnets, a beam loss monitor (BLM) covering a large solid angle from the point of beam losses is highly desirable. A BLM that uses a Cherenkov radiator plate wrapping around the beam pipe is utilized in the Linac Coherent Light Source (LCLS) undulators, and a similar BLM geometry has been tested for the Advanced Photon Source (APS) undulators. We report on measurements made with these BLMs recently installed in the APS storage ring and the booster-to-storage-ring transfer line. A two-order-of-magnitude variation in the relative sensitivity of the Cherenkov detector is observed as a function of incident electron position in the quartz radiator. A factor of 10 variation in signal sensitivity was observed with the change of particle entry angle. The introduction of tungsten and lead shields enhances count rates by 30 – 40%. When the detector is moved along the insertion device chamber, the signal intensity peaks 1 m from the chamber entrance. The measured data are compared with numerical simulation of the beam loss processes.

## INTRODUCTION

At the APS, a large area beam loss monitor (BLM) was developed for the LCLS to measure radiation dose rates at the FEL undulator magnets [1]. The BLM detects Cherenkov radiation generated by high-energy electrons in an aluminum-coated, quartz radiator. The radiator is placed just upstream of each LCLS undulator magnet. Ray-tracing analyses and numerical simulations show that the optical efficiency varies by at least 2 orders of magnitude as a function of electron position in the radiator [2]. In this work, we present detector efficiency measurements using APS high-energy radiation beams.

## BEAM LOSS MONITOR DESIGN

Figure 1 shows the tuning-fork-shaped LCLS-BLM radiator design. The electron beam passes into the paper at the location of the small cross in the figure. The radiator wraps around the beam pipe and covers the entire area of the undulator magnets. Shower particles from high-energy, lost electrons are expected to deviate only slightly from the incoming beam direction and enter the radiator approximately normal to the surface of the paper.

Figure 2 shows the enlarged top view of the coupling area between the radiator and the photomultiplier tube (PMT). The Cherenkov radiation is emitted in a cone with a half cone angle determined by  $\cos\theta_c = 1/n\beta \approx 1/n$ , where  $n \approx 1.47$  is the refractive index of the radiator material. In our case,

where the PMT is mounted  $90^\circ$  from the direction of the electron beam,  $\theta_{\text{PMT}} = \pi/2 - \theta_c$ , and  $\sin\theta_{\text{PMT}} \approx 1/n$ , which is the same condition of total internal reflection at the PMT coupling surface, implying a very low coupling efficiency with the PMT. We note that the condition of total internal reflection can be broken if the radiator is rotated.

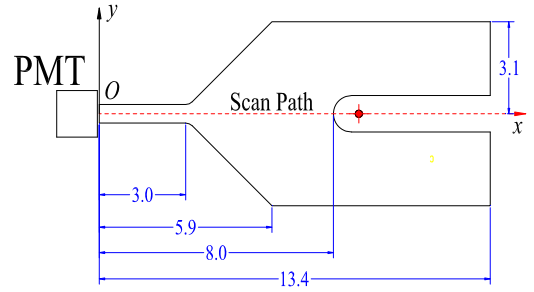


Figure 1: BLM radiator (units in cm). The dashed line shows the scan path of the gas bremsstrahlung beam.

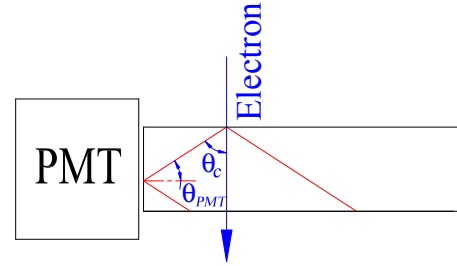


Figure 2: Top view of the radiator showing the Cherenkov radiation cone and the total internal reflection.

## GAS BREMSSTUHLUNG SOURCE

Undulators occupy many long straight sections in synchrotron radiation sources. As stored electrons traverse through the residual gas in these straight sections, gas bremsstrahlung (GB) photons are generated with energies up to the electron energy of the machine [3-6]. During normal operations, the GB photon beam is stable with a well-defined direction, size, and intensity. Accessibility to experimental stations makes it possible to perform experiments with high-energy, gamma-ray and electron detectors with great flexibility and convenience. We hope to demonstrate the advantages of this gamma-ray source for testing radiation detectors using, for example, pair-production electrons and photoneutrons.

## Simulated Angular Distribution

To characterize the GB radiation in the 35-IDA hutch, realistic beamline geometry is simulated using the

\* Work supported by U.S. Department of Energy, Office of Science, Office of Basic Energy Sciences, under Contract No. DE-AC02-06CH11357

particle tracking code MARS [7,8]. Since the scattering angle  $1/\gamma$  dominates the size of the GB photon beam in the x-ray hutch, a circular electron beam was assumed for simplicity the left side of Figure 3 shows a scatter plot of (right) simulated photon distributions. The adjacent plot shows the distribution of photons with a 0.8-cm-thick tungsten block placed just upstream. From these data sets, intensity profiles can be calculated.

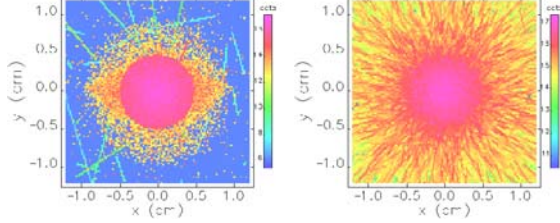


Figure 3: Left: MARS-simulated GB photon plot; Right: GB plot with a 0.8-cm-thick tungsten block.

### Measured Spatial Distribution GB Beam Source

The transverse GB radiation profiles are measured using two additional reference detectors of different design located 38 m from the center of the straight section: 1) a Bergos PIN diode beam loss monitor [9] and 2) a lead-encased Cherenkov detector (CD) [10,11]. Both detectors are running in pulse-counting mode.

Figure 4 shows the horizontal and vertical intensity profiles acquired with the Bergos diode. The spatial distribution of MARS-simulated gamma-ray fluence is plotted for comparison, after normalization at the peak. While the FWHM of the Bergos profiles measure 3 mm horizontally and 2.3 mm vertically, the FWHM of simulated profile measures 4.2 mm. The simulation is not detector-specific; therefore, the agreement between these data sets is considered reasonable.

Figure 5 shows the horizontal and vertical intensity profiles acquired with the reference CD. The spatial distribution of the MARS-simulated gamma-ray fluence with the 0.8-cm-thick tungsten block just upstream of the detector is plotted for comparison, after normalization at the peak. The FWHM of the Cherenkov profiles are measured to be 13 mm in both directions; whereas, the FWHM of the simulated profile measures only 5 mm. We note that the reference CD uses a cylindrical radiator, 8 mm in diameter and 10 mm in length, shielded by a lead cylinder 15 mm thick. The size of this CD radiator is large compared to that of the beam, which contributes to the poor spatial resolution. We note that since the PMT is mounted on top of the radiator [11], the asymmetric profile shows the transport efficiency of Cherenkov radiation is reduced as the GB beam is scanned away from the PMT ( $x < 0$ ).

Figure 6 shows a vertical scan of the CD over a wider spatial range. We can see that the measured radiation has long exponential tails away from the central peak. This broad wing appears to be related to the additional beam losses associated with APS storage ring top-up injection.

## GB RADIATION MEASUREMENT

The LCLS BLM was mounted on an  $XY\theta$  stage to map out the detector efficiency as a function of the electron entry point coordinates and entry angle. The BLM is rotated along the vertical axis,  $y$  in Figure 1. The PMT rotates downstream of the axis when  $\theta > 0$ .

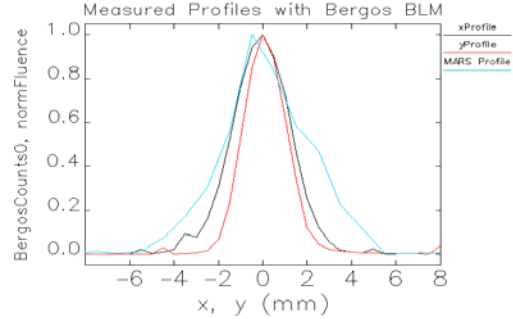


Figure 4: Measured horizontal and vertical profiles using a Bergos BLM, along with a MARS-calculated gamma-ray fluence profile for comparison.

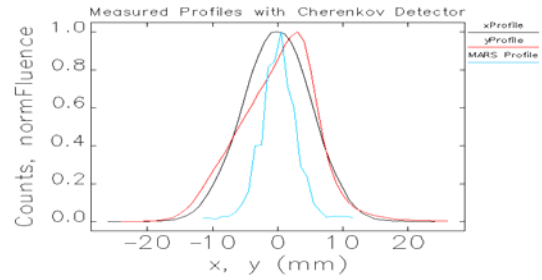


Figure 5: Measured horizontal and vertical profiles using a Cherenkov detector, along with a MARS-calculated gamma-ray fluence profile for comparison.

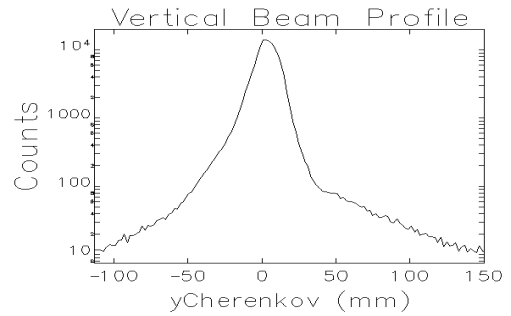


Figure 6: Measured vertical profile over an increased spatial range using a Cherenkov detector.

### Measured Angle Dependence

Figure 7 shows the count rate as a function of  $x$  when the entry point is scanned along the path shown in Figure 1. A 12.5-mm brass plate was placed 15 cm upstream of the detector to enhance the shower. We observe the following features in the data: (1) The change in slope at  $x = 30$  mm correspond to the end of the narrow neck in the radiator; (2) the slope variation at  $x = 80$  mm corresponds to the cut-out for beam pipe; (3)

counts beyond  $x = 80$  mm are likely a result of scattering from the brass enhancer. We can see that the collection efficiency is a very sensitive function of the entry position. It decreases by a factor of 200 when the entry point is scanned horizontally from the PMT to the beam pipe. The collection efficiency is also a sensitive function of beam entry angle. Outside of the narrow neck, it increases over 20 times when the radiator is rotated by +39 degrees.

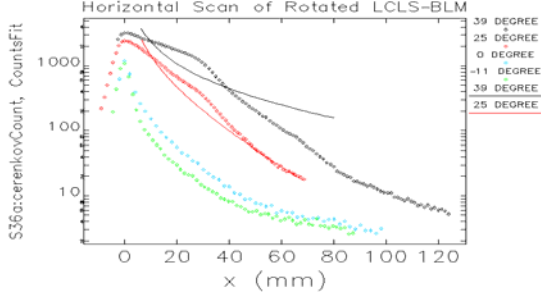


Figure 7: BLM sensitivity along the horizontal scan path for differing rotation angles (diamonds). Also shown are fits to a parallel plate model for the two larger angles with fit parameter  $R = 0.45$ .

### Parallel Plate Approximation

Next we apply the parallel plate model [2] for the experimental geometry. Figure 8 shows an electron entering the radiator at an incident angle  $\theta_i$  and generating a Cherenkov light cone around the particle trajectory. We trace the Cherenkov rays propagating towards the PMT through multiple reflections Q-R-S-T. To calculate the length, we reflect the radiator boundary planes several times to obtain a virtual quartz stack R0-R1-R2-R3-R4, although the Cherenkov light is only generated in R0. We extend the original light ray to intercept the virtual radiator exit aperture at P-Q-R'-S'-T'-U'. By the time the ray reaches the end of the radiator,

the Cherenkov cone radius is  $x' = x - \frac{d}{2} \sin \theta_i \approx x$ ,

where  $x \gg d \sin \theta_i$ . The height of the cone is given by

$y' = x' \cot(\theta_i + \theta_c)$  and the number of reflections is

given by  $n_R = \left[ \frac{y'}{d} + \frac{1}{2} \right] \approx \frac{y'}{d}$ , where  $d$  is the thickness

of the radiator, and the fraction of light cone intercepted by the PMT is  $D / 2\pi x'$ , where  $D$  is the PMT diameter.

For surface reflectivity  $R$ , the light intensity at the PMT is  $I(\theta) \propto \frac{DT_{PMT}}{2\pi x' \cos \theta_i} R^{n_R}$ , which accounts for the

increased length of the oblique path and the transmittance for in-plane polarized light at the exit

aperture [12],  $T_{PMT} = \frac{4n \sin(\theta_i + \theta_c) \cos \theta_i}{[\sin(\theta_i + \theta_c) + n \cos \theta_i]^2}$ .

Hence

$$I(\theta) \approx I_0 \frac{T_{PMT}}{x \cos \theta_i} R^{x/d \tan(\theta_i + \theta_c)}. \quad (1)$$

The two parameters,  $I_0$  and  $R$ , can be adjusted to measured data fit in this expression. We found that low values of  $R < 0.6$  are needed to account for the steep slopes in Figure 7. We acknowledge that this reflection coefficient is unrealistically low. Further refinement of the model to correlate the fluence with count rate is required.

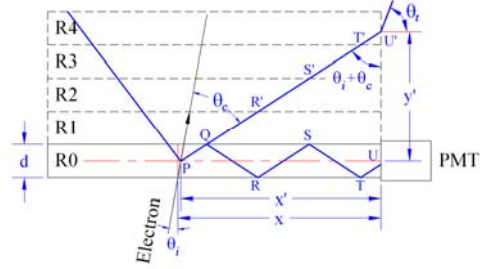


Figure 8: Parallel plate approximation of the transport of Cherenkov light.

### STORED BEAM LOSSES

The tuning fork design was considered an attractive candidate for APS undulator magnet dosimeters because of the radiator's large solid angle. A larger fork fitting the APS insertion device (ID) chamber has been built and installed at Sector 33. The detector is configured in pulse-counting mode, recording single electron losses due to Touschek scattering, as well as injection losses at the chamber entrance. A CD next to the ID chamber is used to monitor the local electron losses (flux monitor). The data are averaged over five-day-long user runs. Only 24-bunch fill patterns are used since different magnetic lattices give slightly different loss profiles, likely from different spatial distribution of the lost electrons.

### Shielding Dependence

A 10-mm-thick tungsten shielding plate and another 3-mm lead plate, are installed upstream of the BLM to increase the production of electrons in the electromagnetic shower. Table 1 lists the count rate of the detector  $N_{TF}$ , that of the CD  $N_{CD}$ , and their ratio  $N_{TF}/N_{CD}$  for three different shielding configurations. We see that the 3-mm lead plate enhanced the count rate by  $\sim 30\%$ ; and the 10-mm tungsten plate enhances by  $\sim 40\%$ .

Table 1: Tungsten Enhancer Effect on BLM Sensitivity

Shielding	$N_{CD}$ (c/s)	$N_{TF}$ (c/s)	$N_{TF}/N_{CD}$
No Shielding	54.9	405	6.0 (baseline)
3-mm lead plate	51.2	339	7.9 (+30%)
10-mm tungsten	60.1	501	8.3 (+40%)

### Distance Dependence

The BLM, with a 10-mm tungsten shield, was positioned at four different locations along the ID chamber over the course of 3 months. Table 2 compares the measured ratio  $N_{TF}/N_{CD}$  at four different locations;

the distance was measured from the ID chamber entrance. While the flux monitor shows that the loss rate is stable within  $\pm 20\%$ , the TF-BLM signal changed over  $\pm 100\%$ . The TF-BLM count rate reaches a maximum at 0.86 m and then starts to decrease; indicating that a significant number of particles emerge from the ID chamber at angles greater than 30 mrad. These electrons could then possibly pass over the BLM located at  $z = 1.3$  m.

Table 2: BLM Count Rate as Function of Position

Location (m)	$N_{CD}$ (c/s)	$N_{TF}$ (c/s)	$N_{TF}/N_{CD}$
0.00	47.5	308	6.5
0.86	66.8	1642	24.6
1.30	70.3	1276	18.1
1.73	56.3	633	11.3

MARS simulations were performed using Sector 33 geometry without the undulator. Since we had no prior knowledge on the lost electron distribution, two cases were modeled: (1) a “thick beam,”  $\sigma_x = 1.5$  cm,  $\sigma_y = 0.5$  cm, and (2) a “thin beam,”  $\sigma_x = 1.5$  cm,  $\sigma_y = 0.1$  cm. Figure 9 shows the integrated electron fluence in the BLM radiator as a function of radiator position  $z$ . While both profiles peak in the first meter, the thin beam has the more pronounced peak. Near the chamber entrance, the shower cone is small, so the lower efficiency of the detector could suppress the measured count rate. As  $z$  increases, the shower expands and more particles hit the BLM near the PMT end, thus increasing the count rate. This could partly explain the difference between Figure 9 and Table 1.

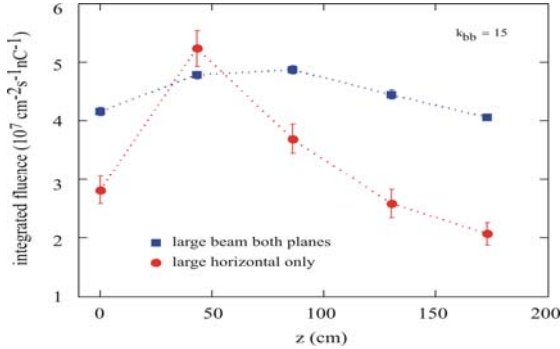


Figure 9: Simulated axial profiles of electron fluence in the BLM radiator versus position along the ID vacuum chamber. Tungsten enhancer is presented.

Figure 10 shows the enhancement ratio of the tungsten plate at different locations. At the chamber entrance, when the average electron energy is low, the tungsten plate actually reduces the electron fluence in the BLM. As  $z$  increases, more energetic electrons emerge from the chamber after smaller-angle scattering, and the fluence downstream of the tungsten plate increases dramatically. At  $z = 1.73$  m, the electron fluence is 150% higher with the tungsten plate than without it. This compares with the observed count rate enhancement of 40% in Table 1. At this time, it is not clear to us how the fluence enhancement translates to a pulse count rate increase, and the direct comparison is difficult.

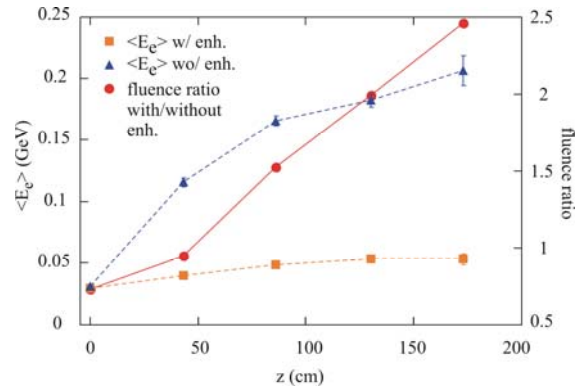


Figure 10: Fluence enhancement ratio by a 10-mm tungsten plate (circle); Electron fluence in BLM with W-plate (triangle) and without it (square).

## BTS MEASUREMENTS

Two 0.5-mm thick chromium-doped alumina flags (Chromox screen) are employed to generate localized loss in the 7-GeV transport line from the booster synchrotron to the storage ring (BTS). Depending on which of the two flags are inserted, the loss point occurs either 12 or 20 m upstream of the BLM. As shown in Figure 11, the BLM is mounted on a pneumatically-driven linear slide that raises and lowers the detector out of a lead-brick shield for exposure to scattered electrons. Assuming linear operation of the photomultiplier tube (PMT) we expect the BLM’s PMT, current to follow a power law of applied voltage  $V_{PMT}$ ,

$$G(V_{PMT}) = G_0 \left( \frac{V_{PMT}}{V_0} \right)^{n_p}, \quad (2)$$

where  $n_p = 7.2$  for the 7-stage R7400-04 tube used here. The output charge of the BLM PMT as a function of high voltage bias is shown in Figure 12, along with the power law extrapolation of the charge measured at  $V_{PMT} = 300$  V.

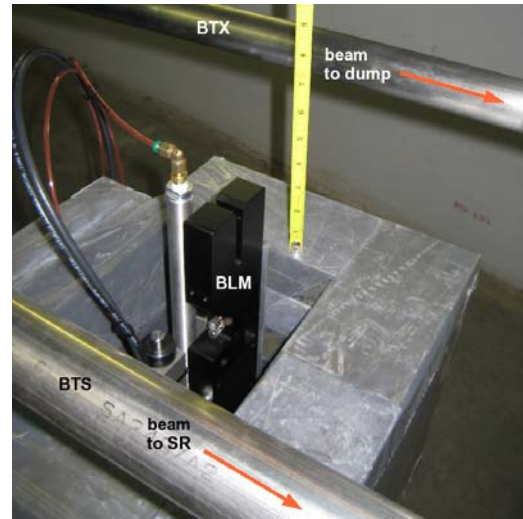


Figure 11: LCLS BLM in the raised position between BTS and BTS beamlines.

MARS simulation was performed for the two scattering geometries, including the quadrupoles fields



upstream of the radiator. To estimate absolute signal intensity, we used the measured charge from the booster synchrotron, the known thickness of the flag, and the small-current PMT gain at 400 V bias, where the PMT appears to be in the linear range. For simplicity, we used a uniform optical coupling of  $3.5 \times 10^{-3}$ , consistent with a reflectivity  $R = 0.9$ . As shown in Figure 12, the results are within a factor of 3 of the measured data. Unfortunately, due to the non uniformity of the BLM response, the result was a large error bar. While the good agreement strengthens our confidence in using MARS as a tool to study APS beam losses and shielding, we note that discrepancies still exist. For example, the simulation is unable to predict the ratio of lost charge at the two flags.

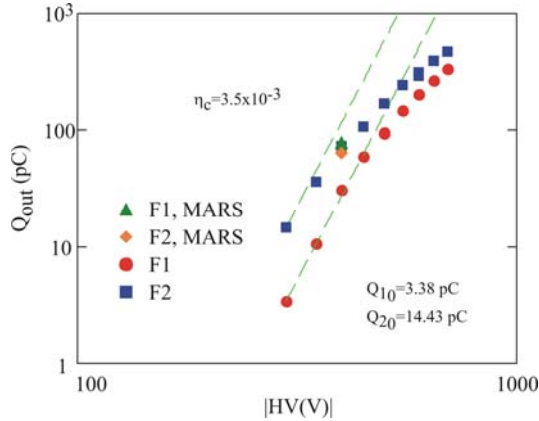


Figure 12: LCLS BLM integrated current signal output as a function of PMT bias voltage. Dashed lines represent power law extrapolation of data at 300 V. It also includes predicted PMT charge for PMT voltage of 400 V, using MARS simulations (diamond and triangle).

## SUMMARY

We measured a tuning-fork shaped, large solid angle BLM at the APS using gas bremsstrahlung beam from the 15-m straight section, Touschek-scattered electrons from the ID chamber, and flag-scattered electrons in the BTS. We found that the TF-BLM efficiency may vary by a factor of 200 for different electron entry points. The count rate is also sensitive to particle entry angle, varying nearly two orders of magnitude over the angle range of  $\pm 40^\circ$ .

We also performed BLM calibration at the BTS transport line with radiation dosimetry. Despite the complex geometry of the BTS, the MARS simulation predicted an absolute signal level within a factor of three.

The GB photon beam at the APS is shown to be a gamma ray source with well-defined size and small divergence and may prove a useful tool for the development and calibration of radiation detectors in the APS accelerators.

We would like to thank Glenn Decker and Louis Emery for their enthusiastic support for this project. We would also like to thank Heinz-Dieter Nuhn, Alan Fisher, and Mario Santana of the LCLS group for stimulating discussions.

## REFERENCES

- [1] W. Berg, J. C. Dooling, A. Pietryla, and B.-X. Yang, "Development of a Beam Loss Monitor System for the LCLS Undulator Beamline," LINAC'08, p. 492, 2008; <http://www.JACoW.org>.
- [2] J. Dooling, these proceedings.
- [3] N. Ipe, D.R. Haeffner, E.E. Alp, S.C. Davey, R.J. Dejus, U. Hahn, B. Lai, K.J. Randall, and D. Shu, "Guide to Radiation Beamline Shielding Design at the APS," ANL/APS/TB-7 (1993).
- [4] P. K. Job, et al. "Guidelines for Beamline and Front-End Radiation Shielding Design at the Advanced Photon Source," ANL/APS/TB-44, Rev. 3, September 2008.
- [5] M. Pisharody, E. Semones, and P. K. Job, "Dose Measurements of Bremsstrahlung-Produced Neutrons at the Advance Photon Source," ANL/APS/LS-269 (1998); Nucl. Instrum. Meth. A, 430, 542 (1999).
- [6] J. C. Dooling, "Dose Calculations Using MARS For Bremsstrahlung Beam-Stops and Collimators in APS Beamline Stations," ANL/APS/TB-54, 2010.
- [7] N. V. Mokhov and S. I. Striganov, "MARS15 overview," Technical Report Fermilab-Conf-07/008-AD, 2007.
- [8] N. V. Mokhov et al., "Physics models in the MARS15 code for accelerator and space applications," in Int. Conf. on Nuclear Data for Science and Technology, AIP Conf. Proc. 769, pp. 1618-1623, 2004.
- [9] K. Witteburg, "Beam Loss Monitor for the HERA proton Ring," EPAC'90, p. 789, (1990); <http://www.JACoW.org>.
- [10] A. Fischer et al., "Diagnostics Development for the PEP-II B Factory," AIP Conf. Proc. 390, BIW'96, p. 248 (1996).
- [11] A. Pietryla, W. Berg, "A Cerenkov Radiation Detection System for the Advanced Photon Source Storage Ring," PAC'01, p. 1622, (2001).
- [12] P. Lorrain and D. Corson, *Electromagnetic Fields and Waves*, 2<sup>nd</sup> ed., Freeman, San Francisco, 1970.